Production of Core/Shell Fibers by Electrospinning from a Free Surface

Keith M. Forward[1,2], Alexander Flores[1] and Gregory C. Rutledge[1]

[1] Department of Chemical Engineering,
Massachusetts Institute of Technology, Cambridge, MA 02139
[2] Department of Chemical And Materials Engineering,
California State Polytechnic University, Pomona, Pomona, CA 91768

Abstract

Electrostatic fiber formation ("electrospinning") is the leading technology for production of continuous fibers with submicron diameter. Applications such as drug delivery and sensors benefit from the ability to produce submicron fibers with a core/shell morphology from electrified coaxial jets of two liquids. However, low productivity of the conventional needle-based coaxial process is a barrier for commercialization. We present a novel technology that overcomes this limitation by the development of coaxial jets directly from compound droplets of immiscible liquids entrained on wires, and control of mass transfer processes to produce uniform, core/shell fibers. The enabling feature of controlled evaporation by design of solution properties is verified by a simple mass transfer model. Electron micrographs confirm the formation of fibers with the desired morphology. The proposed technology creates the opportunity to produce nanofibers with core/shell morphology on an industrial scale for a wide variety of applications.

1. Introduction

Nonwoven mats of electrospun fibers are remarkable for their unusual combination of high porosity, high surface area and small diameter fibers. Electrospun fibers with core/shell morphology comprise an important subset of these materials, characterized by distinct interior and exterior compositions. These materials are promising for a broad range of uses, including filtration, tissue engineering, nanocomposites, smart textiles and alternative-energy applications such as solar cells, fuel cells, and energy storage devices (Yarin, 2001; Moghe and Gupta, 2008).

Electrospun core/shell fibers are produced conventionally by a method called coaxial electrospinning, a simple technique that employs two concentric spinnerets ("needles") to feed fluids to a coaxially jetting stream, resulting in core/shell fibers ranging from 0.1 to 10 micrometers in diameter (Sun et al., 2003; Yu et al., 2004; Li and Xia, 2004). One of the major drawbacks of the conventional process, for both single and multiple fluids, is the limited productivity, typically around 0.001 to 0.1 g/h per spinneret (Theron et al., 2004; Rutledge and Fridrikh, 2007). Attempts to develop multi-spinneret configurations have shown limited success (Theron et al., 2005). A number of alternative high-productivity configurations in which electrohydrodynamic (EHD) jets are emitted directly from a free liquid surface have been reported for single fluids (Niu and Lin, 2012). These configurations go by various names, including "needle-less" electrospinning (Yarin and Zussman, 2004; Niu et al., 2009; Miloh et al., 2009; Kostakova et al., 2009; Jirsak, 2010) and "bubble" electrospinning (Liu and He, 2007; Varabhas, 2009) and differ in the manner by which a jet is emitted from the free surface of a

charged liquid. We refer to these techniques collectively as "free surface electrospinning". Free surface electrospinning is capable of producing fibers at rates that are two to three orders of magnitude higher than spinneret-based methods (Yarin and Zussman, 2004). However, these free surface methods are not readily generalized to multiple fluids. To date, none of them have been shown capable of producing fibers with core/shell morphology. An interesting intermediate process is the recently described "slit electrospinning" technique (Yan et al., 2012).

Here, we report free surface electrospinning from a wire electrode, where metal wire electrodes are mounted on a spindle and drawn through a liquid bath, as shown in Fig. 1(a). This process has been studied previously for a liquid bath comprising a single liquid (Forward and Rutledge, 2012). We introduce a new bath configuration comprising two immiscible liquids, layered one on top of the other. The wire electrodes are oriented parallel to the liquid surface. The liquids are solutions consisting of one or more volatile solvents and nonvolatile solutes. As the wire sweeps through the bath, first the bottom liquid, then the top liquid, becomes entrained on the wire. This configuration leads to the formation of an annular bilayer film on the wire, wherein the bottom liquid coats the wire and the top liquid coats the bottom liquid. Due to the Plateau-Rayleigh instability, the bilayer film breaks up into individual droplets on the wire, each droplet containing the bottom liquid encapsulated within the top liquid. When the droplets are charged in the presence of an electric field, they orient themselves toward the downfield side of the wire electrode and deform into individual Taylor-like cones. At sufficiently high electric fields, each droplet emits a charged jet with the liquids arranged coaxially within the jet. As the jet travels toward the grounded collector, it stretches and thins, primarily due to electric field-induced stresses and charge repulsion. The volatile solvents from the two liquids evaporate in a controlled manner from the coaxial jet to produce solid fibers with a uniform, core/shell morphology. Success of the method depends nontrivially on the design of the two fluids to ensure that entrainment, jetting and drying occur in the desired manner, as described below.

2. Materials and methods

To demonstrate this process, submicron diameter core/shell fibers were produced from a variety of solution pairs. Experiments were carried out using solutions of 300kDa polyethylene oxide (PEO) and 35kDa polyethylene glycol (PEG), 360kDa polyvinylpyrrolidone (PVP) or 1.3MDa PVP in deionized (DI) water as the bottom liquid. Solutions of 35kDa polystyrene (PS) in mixtures of n-butanol and mesitylene were used as the top liquid. All chemicals and solvents (except for DI water) were obtained from Sigma Aldrich. The solution conductivities were measured using a VWR Digital Conductivity Meter. The liquid-liquid interfacial tensions were estimated by a reciprocal solubility method (Donahue and Bartell, 1952), and values of liquid-vapor surface tensions were obtained from the literature (Pan et al., 2004). The viscosity was determined by an AGR2 Rheometer (TA instruments) with a cone and plate configuration and a shear rate between 0.1-1000 s^{-1}.

Different concentrations of the co-solvent, n-butanol, in the top liquid were used to modulate the solubility of the two solvents. The equilibrium solubility data for the ternary solvent system of water, n-butanol and mesitylene was obtained from the literature (Shrzecz et al., 1999). As the concentration of n-butanol in the top liquid increases, the solubility of water also increases. At concentrations of n-butanol higher than 35 wt%, a second, polystyrene-rich phase forms within the solvent-rich phase; for this reason, the concentration of n-butanol in mesitylene was kept below 35 wt%. Solution compositions used in this work, and their properties, are reported in the Appendix Tables A1 and A2. The top organic liquid was of lower

density than the bottom aqueous liquid in all cases, so that layering of the liquids in the bath was maintained as two distinct phases throughout the experiment.

During electrospinning, the grounded collector plate was placed above the bath/spindle apparatus, so that, the distance between the collector and wire electrodes (radius of 100 microns) was 30 to 35 cm; this distance allows enough time for the majority of the solvents to evaporate from the liquid jet before impaction on the collector. The rotation rate of the spindle was controlled in the range of 2.5-12 rpm by a small DC motor. For a spindle diameter of 3.2 cm, this corresponds to a wire velocity in the range 4 – 20 mm/s. The applied voltage was controlled by a Gamma High voltage power supply (model RR40-1.5) and ranged from 30 to 38.5 kV. Both the liquid bath and wire electrodes were connected to the high voltage power supply. Solution aging (i.e. change of composition due to evaporation of solvent from the surface of the bath) was not significant because the top fluids have relatively low vapor pressures relative to other solvents commonly used for electrospinning. Nevertheless, for the results reported here, experiments were limited to 20 minutes or less and were performed in a closed chamber with a temperature ranging from 21-24 °C and a relative humidity less than 2%. Further details of the experimental apparatus may be found in ref 18 (Forward and Rutledge, 2012).

UV-Vis spectrometry (PerkinElmer Lambda 35 UV-vis spectrometer) was used to measure the adsorption intensity of electrospun fibers at 260 nm, where polystyrene is UV active. A calibration curve for intensity versus PS concentration was prepared using solutions of known concentrations of PEO and PS, or PVP and PS, in dichloromethane (DCM). At least 50 mg of electrospun material was dissolved in DCM to produce a PS concentration below 0.35 mg/mL; at higher concentrations, the intensity of the signal saturated. The prepared solutions were placed in a quartz cuvette, and the intensity of absorbance was measured for wavelengths from 200 to 400 nm. The other polymers and solvents used in this work (PEO, PEG, PVP, water, n-butanol and mesitylene) are not UV active in the range of interest. The electrospun mats were allowed to dry for at least a day to ensure that any residual solvent was removed. The fibrous mats were examined by scanning electron microscopy (SEM) to study fiber morphology. In addition, SEM micrographs of fractured fibers and transmission electron micrographs (TEM) of individual electrospun fibers confirm the desired core/shell fiber morphology. Fiber diameters were measured from SEM micrographs using ImageJ software (National Institute of Health, 2012). A simple transport model is proposed to explain the observed fiber morphologies.

3. Results and discussion

First, to ensure layering of the liquids and formation of compound droplets without mixing, the liquids must be immiscible. Immiscible solutions have been investigated previously in the conventional electrospinning process to produce coaxial jets, but these systems have resulted invariably in the formation of hollow and/or collapsed fibers (Longson et al., 2001; McCann et al., 2005). To produce uniform core/shell fibers free of voids, the core phase solvent must diffuse through the shell phase and evaporate at the outer surface of the jet on a time scale commensurate with the evaporation of the shell phase solvent. For this reason, reports of conventional coaxial electrospinning to form fibers with core/shell morphology employ solvents that are miscible with each other and with the shell polymer. In cases where the diffusion of core solvent through the shell is incomplete, fibers may contain a large amount of voids, and/or form collapsed, ribbon-like fibers. Such fiber morphologies were observed by Koombhongse *et al* (Koombhougse et al., 2001) and analyzed by Pai and co-workers (Pan et al., 2009; Wang et al., 2009) for single fluid systems. Here, we solve the problem of generating core/shell fibers from

coaxial jets of immiscible solutions through the introduction of co-solvent to modulate the solubility of the core solvent in the shell solution.

Second, the entrainment of both liquids on the wire depends on the capillary number ratio of the two liquids. It is well known that as a thin cylinder is drawn through a deformable fluid interface, the thickness of the annular film of entrained fluid, h, is a function of the capillary number Ca of the fluid, according to the relationship $h \sim Ca^b$ when $Ca < 1$ (Quéré, 1999). $Ca = u\eta/\gamma$, where u, η, and γ are the velocity of the cylinder, viscosity of the fluid and the interfacial tension between the two fluids, respectively. Here, we draw the wire through two immiscible liquids in succession, resulting in entrainment of each to form a bilayer film on the wire, as illustrated in Fig. 1(b). Typically, the thickness of the entrained bilayer film (h_B+h_T) is small compared to the radius of the wire (100 microns) (Forward and Rutledge, 2012). To a good approximation, the volume fraction of the bottom liquid, ν_B, on the wire varies with the ratio of the capillary numbers of the top and bottom liquids, Ca_T/Ca_B, (where the subscripts "T" and "B" denote top and bottom liquids, respectively) according to Eq. (1):

$$v_B \approx \frac{h_B}{h_B + h_T} = \left[1 + \left(\frac{Ca_T}{Ca_B}\right)^b\right]^{-1} \qquad (1)$$

For the case where the axis of the wire is oriented parallel to the liquid surface, we have previously shown empirically that $b = 0.21 \pm 0.011$ (Forward and Rutledge, 2012).

Fig. 1(c) shows the experimentally determined volume fractions of the bottom liquid in the entrained bilayer film, from UV-Vis measurements, as a function of Ca_T/Ca_B, according to Eq. 1. The relative amounts of solution entrained on the wire during processing were obtained from mass balances applied to each polymer in the final nonwoven mat. When Ca_T/Ca_B is much larger than unity, the bottom fluid is "swept off" of the wire by the top fluid. When Ca_T/Ca_B is much smaller than unity, the top fluid experiences insufficient viscous forces to be entrained on the bottom fluid. Similar behavior has been observed in simulations of a rigid sphere passing through a deformable interface between two fluids (Geller et al., 1986). The experimental data shows good agreement with Eq. 1 over three orders of magnitude of capillary number ratio, from 0.001-1. Fig. 1(c) also confirms that the composition of the entrained liquid has no apparent dependence on the rotation rate of the wire spindle, due to the cancellation of velocities in the capillary number ratio. This shows that the relative amount of each entrained liquid depends primarily on the solution properties of the two liquids and not the production rate (*i.e.* electrode rotation rate).

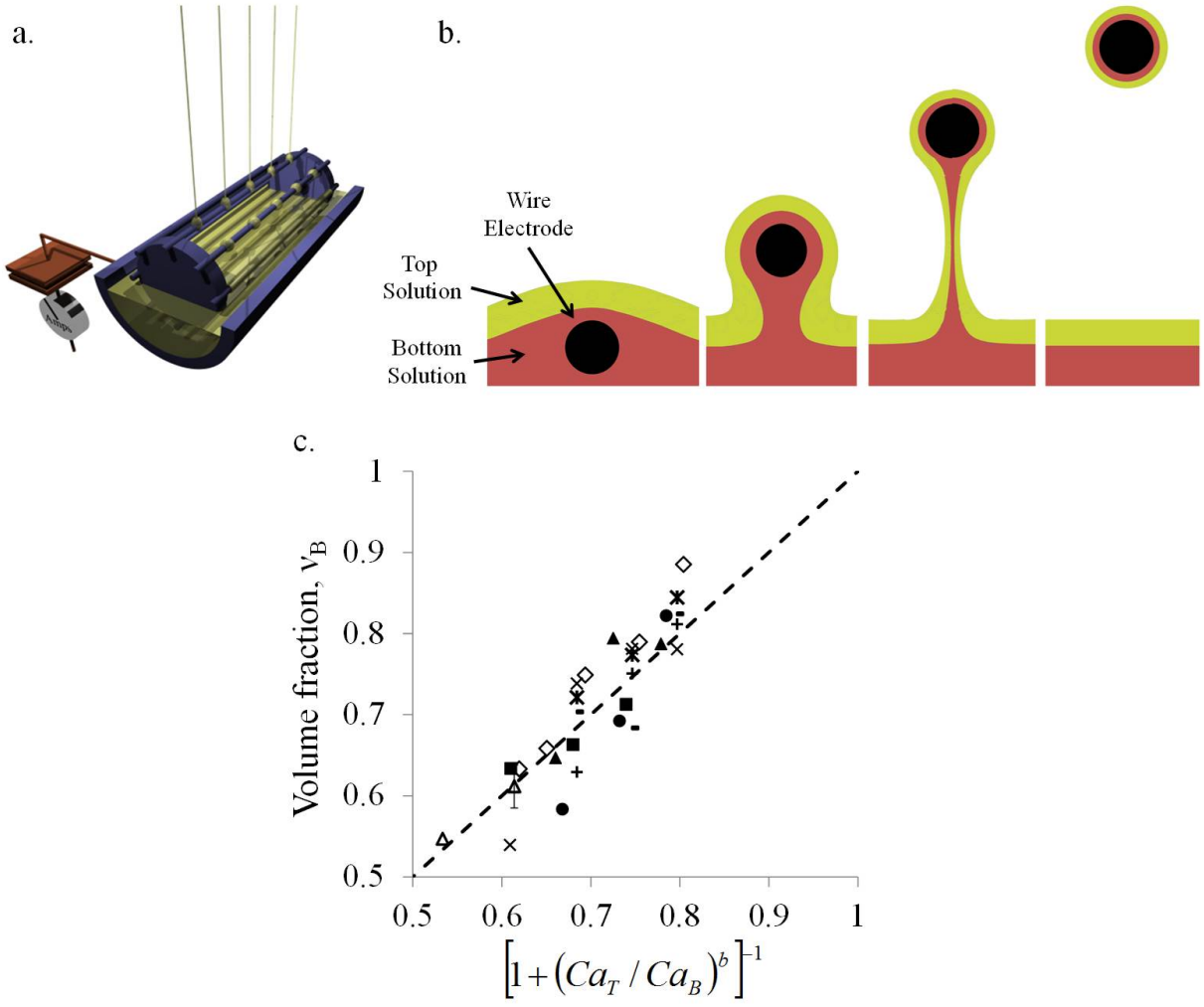

Figure 1. (a) Free surface electrospinning from wire electrodes, illustrated for a single liquid. The liquid bath (gold) is charged to a high voltage. As the spindle of wires rotates counterclockwise (as viewed here), the entrained solution first forms a film as shown on the first (leftmost) wire, which then breaks up into droplets as shown on the second (middle) wire. As the spindle rotates, the electric field at the wire increases, so that each droplet emits a fluid jet as shown on the third (rightmost) wire. Evaporation of solvent results in the formation of dry fibers. (b) Evolution of the surface profiles of the two immiscible liquids as the wire (viewed end-on) travels through the liquid interfaces. (c) The volume fraction of the bottom liquid in the entrained bilayer films as a function of the capillary number ratio of the two liquids. The dashed line is the relation given by Eq. 1, with b = 0.21. The open symbols were obtained from experiments in which the bottom liquid was 8 wt% 1.3MDa PVP (triangles) or 15wt% 360kDa PVP (diamonds) in DI water, with top liquids of varying concentrations of 35kDa PS in a 35:65 mixture (by weight) of n-butanol and mesitylene. The filled symbols were obtained from experiments in which the bottom liquid was 12wt% PEO+PEG (a 73:27 mixture by weight of 35kDa PEG and 300kDa PEO) in DI water, with top liquids of varying concentrations of 35kDa PS in pure mesitylene (squares), a 10:90 mixture of n-butanol: mesitylene (triangles) or a 20:80 mixture of n-butanol: mesitylene (circles). In all of these cases, the rotation rate was 5.6 rpm. The

remaining symbols are from experiments with a bottom liquid of 12wt% PEO+PEG (the 73:27 mixture) in DI water and top liquid of 10, 20, and 30wt% of 35kDa PS in the 35:65 mixture of n-butanol:mesitylene at rotation rates of 2.5 rpm (x), 5.6 rpm (+), 8.9 rpm (-) or 11.8 rpm (*).

Third, in order to form a coaxial jet from each droplet on the wire, it is desirable to design the more viscous (*i.e.* bottom) fluid to have the higher conductivity. Since the electrical stresses responsible for jet formation arise due to accumulation of charges at interfaces, in accord with the leaky dielectric model (Saville, 1997), this ensures that the more viscous fluid jets first and then entrains the less viscous fluid, in a kind of coating flow. If the charges accumulated instead at the surface of the top fluid, the top fluid would jet first, possibly failing to entrain the bottom fluid. For this reason, in the experiments performed here, the conductivity and dielectric constant of the bottom solutions are greater than those of the top solutions, to ensure that charges build up at the liquid-liquid interface.

Finally, the morphology of the fibers varies with the composition of the core (bottom) and shell (top) liquids. A series of scanning electron micrographs of (PEO+PEG)/PS mats formed using shell liquids with different concentrations of co-solvent, n–butanol, and polymer are shown in Fig. 2. As the concentration of n-butanol was increased (from left to right in Fig. 2), the deposited fiber mats change in appearance from highly fused, irregular, ribbon-like filaments to more uniform, smaller diameter fibers. These micrographs demonstrate the significant impact that shell solvent composition has on the final fiber morphology.

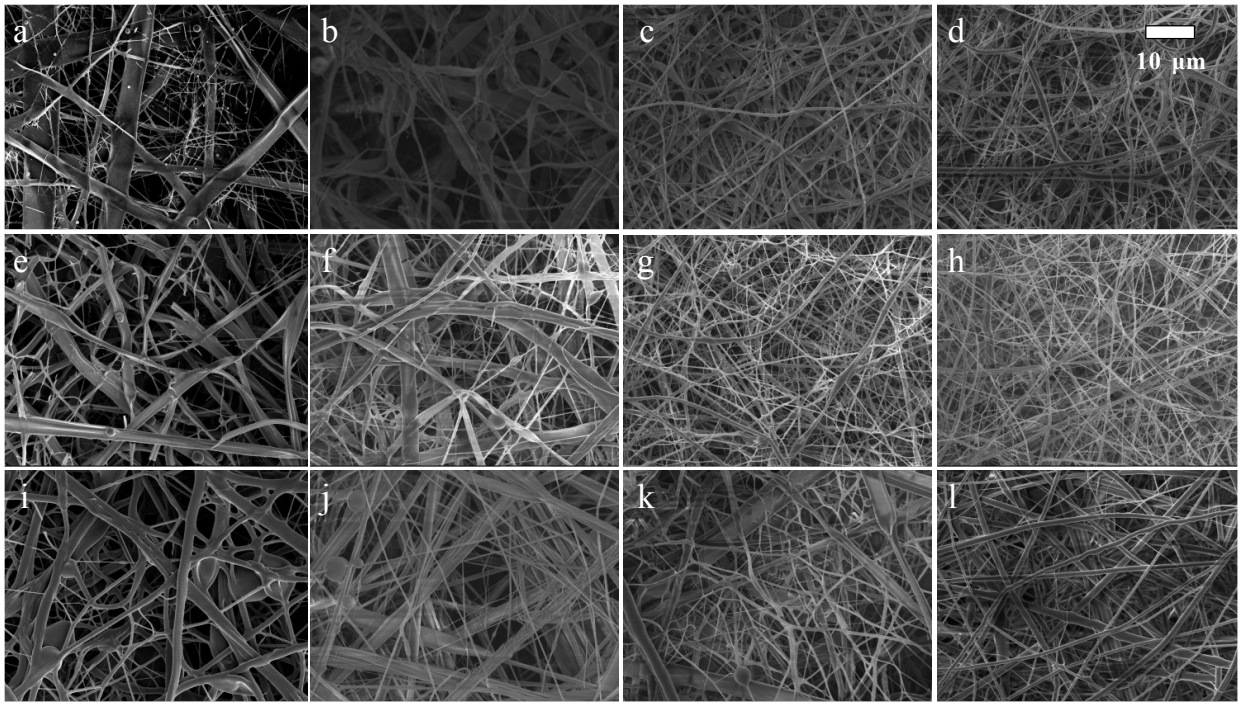

Figure 2. Scanning electron micrographs of fiber mats produced by coaxial free surface electrospinning. The core liquid was 12wt% PEO+PEG (73:27 wt% mixture) in DI water, and the shell liquid was 10wt% 35kDa PS (a, b, c, d), 20wt% 35kDa PS (e, f, g, h) or 30wt% 35kDa PS (i, j, k, l). The shell solvent compositions were pure mesitylene (a, e, i), a 10:90 mixture (by weight) of n-butanol:mesitylene (b, f, j), a 20:80 mixture (by weight) of n-butanol:mesitylene (c,

g, k) or a 35:65 mixture (by weight) of n-butanol:mesitylene (d, h ,l). Ribbon-like fibers are observed in systems a, b, e, f, i, j and k. Uniform fibers are observed in systems c, d, g, h and l.

The morphological variation exhibited by Fig. 2 is a consequence of the order in which the core and shell phases solidify. The time required to solidify the core phase, t_c, depends on the core solute concentration and the rate at which the solvent of the core phase solubilizes into and diffuses through the shell phase, to evaporate eventually at the outermost surface. The time required to solidify the shell phase, t_s, depends on the shell solute concentration and the rate of evaporation of shell solvent. If $t_c > t_s$ the shell phase solidifies first, subsequently buckling as the core continues to shrink, producing ribbons (Wang et al., 2009, Pai et al., 2009). However, if $t_s > t_c$ the core solidifies first, forming a foundation upon which the shell subsequently solidifies, to form the desired core/shell fibers. To confirm this, a simple mass transport model is used to calculate t_c and t_s. The model assumes a cylindrical coaxial jet where the core solvent (water) diffuses through the shell solvent and all solvents (both core and shell) evaporate at the outermost surface. The initial diameter ratio of the core and shell phases in the jet, ε_{j0}, is estimated from the composition of the entrained liquid bilayer ($\varepsilon_{j0} = \nu_B^{1/2}$). As the solvents evaporate, the diameter of the core and shell decrease until solidification occurs in one phase or the other. Solidification of either phase is assumed to occur when the solute concentration reaches 90 vol%. Further details of the model are provided in Appendix B.

Fig. 3 shows a plot of parity in the solidification times for core and shell (t_c=t_s) for three different shell solute concentrations, as a function of initial jet diameter ratio ε_{j0} and co-solvent concentration in the shell fluid. Conditions corresponding to points above each curve represent circumstances where the shell solidifies first; subsequent removal of the core solvent leads to buckling of the solid shell and formation of ribbons. Conditions corresponding to points below the curve represent circumstances where the core solidifies first, followed by drying of the shell to encapsulate the core. Superposed on this diagram are experimental results for these fluids.

The mass transport model correctly predicts the fiber morphology of each system. The model relies only upon solution properties and initial geometry. With increasing n-butanol concentration, the solubility of the water in the shell solvent is enhanced. This increases the mass transport of the water through the shell phase, allowing the core to solidify before the shell. The choice of mesitylene is also significant. If the shell solvent is too volatile, the shell phase solidifies before all the water is able to diffuse through it. Choosing a primary solvent (mesitylene) with a low vapor pressure gives the core phase longer time to solidify. The model also shows the role of polymer concentration. A higher polymer concentration in the shell fluid means less shell solvent to remove, so that the solidification time t_s is reduced. Similarly, higher polymer concentration in the core phase reduces the solidification time t_c. The mass transfer model provides valuable insight into the process, and more significantly into the importance of the solution properties.

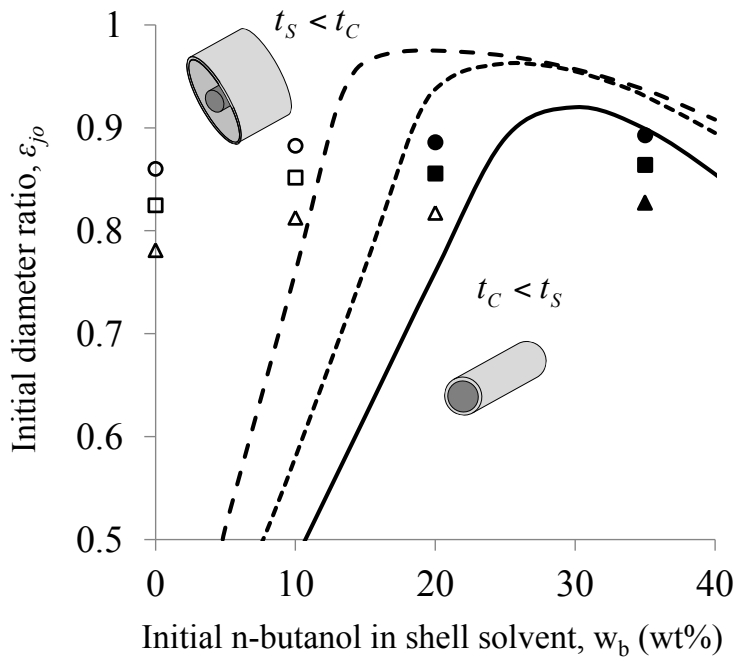

Figure 3. Theoretical diagram of relative solidification times of core and shell, as predicted by the mass transport model. The core solution is chosen to be 12 wt% PEO+PEG (73:27 wt%) in DI water. Each curve represents conditions for which the solidifications times are equal (t_c=t_s) for different polymer concentrations in shell liquid: 10wt% 35kDa PS (long dash), 20wt% 35kDa PS (short dash) and 30wt% 35kDa PS (solid line). Experimental observations from Fig. 2 are superposed on this diagram as follows: 10wt% 35kDa PS (circles), 20wt% 35kDa PS (squares) or 30wt% 35kDa PS (triangles). Open symbols indicate that collapsed ribbons were observed; filled symbols indicate that uniform fibers were observed.

Fig. 4 confirms the successful development of core/shell morphology in fibers produced by the method described here. In the top row of Fig. 4, the SEMs show fibers in which the brittle PS shell has been fractured, exposing the ductile PEO+PEG core. In the bottom row of Fig. 4, a contrast agent (copper (II) chloride) has been added to the core liquid to reveal the core/shell morphology in TEMs.

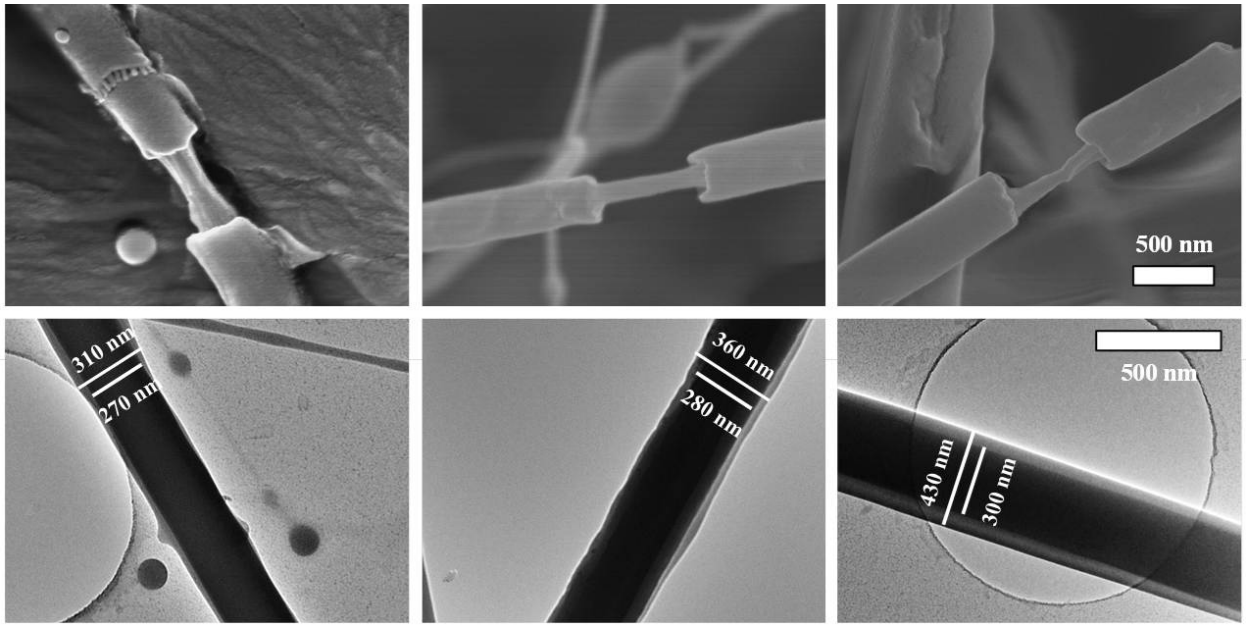

Figure 4. (top row): SEMs of (PEO+PEG)/PS fibers in which the brittle PS shell has been fractured to show the elastic core. From left to right, the images show fibers spun from top liquids of increasing 35 kDa PS concentration in 35:65 mixtures of n-butanol:mesitylene. a) 10wt% PS; b) 20wt% PS; c) 30wt% PS. (bottom row): TEMs of (PEO+PEG)/PS fibers in which 0.2 wt% copper (II) chloride has been added to the bottom liquid. The Cu(II)Cl acts as a contrast agent, revealing the distinct core and shell phases of the fibers. From left to right, the images show fibers spun from top liquids of increasing 35 kDa PS concentration in 35:65 mixtures of n-butanol:mesitylene. d) 10wt% PS; e) 20wt% PS; f) 30wt% PS. In all cases, the bottom liquid was 12wt% PEG+PEO (a 73:27 wt% mixture of 35kDa PEG and 300kDa PEO) in DI water.

The diameters of the core and shell, measured from TEMs, are shown in Table 1. The thickness of the shell increases with increasing polystyrene concentration, due to both the higher viscosity, which results in greater entrainment of the top liquid on the wire (Eq. 1), and the higher concentration of polystyrene in the shell liquid. The ratio of the core diameter to shell diameter in the solid fibers is expressed by the diameter ratio, ε_f. An estimate of $\underline{\varepsilon_f}$ was obtained from the amount of liquid entrained using Eq (2), which was modified from Eq (1) to account for solvent loss. These values are shown in Table 1 along with the ε_f^{exp} observed experimentally by TEM. In general, ε_f is 15-20% greater than ε_f^{exp}.

$$\varepsilon_f = \left[1 + \frac{\rho_B^p \rho_T^f C_T}{\rho_T^p \rho_B^f C_B}\left(\frac{Ca_T}{Ca_B}\right)^b\right]^{-1/2} \qquad (2)$$

Top fluid	Ca_T/Ca_B	ν_B	ε_f	Core diameter (nm)	Shell diameter (nm)	ε_f^{exp}
10wt% PS	0.0020	0.80	0.92	270 ± 110	350 ± 130	0.75 ± 0.06
20wt% PS	0.0074	0.75	0.81	280 ± 150	440 ± 230	0.65 ± 0.08
30wt% PS	0.030	0.68	0.69	350 ± 100	610 ± 160	0.59 ± 0.11

Table 1. The average and standard deviation of the fiber diameter of (PEG+PEO)/PS core/shell electrospun fiber, as well as the theoretical and experimental fiber diameter ratios where the bottom liquid was 12wt% PEG+PEO (73:27 wt% mixture) in DI water and the top liquid was 10, 20 or 30 wt% 35kDa PS in 35:65wt of n-butanol and mesitylene.

4. Conclusion

We have demonstrated for the first time a technique capable of producing submicron electrospun fibers with a solid core/shell morphology from a wire electrode. A simple design equation is presented for the entrainment of two liquids on the wire. The resulting bilayer film breaks up into compound droplets where charges amass at the liquid-liquid interface, so that coaxial jets of both liquids are emitted from each droplet. This technology depends on the careful design of liquids for the core and shell components so that they are immiscible but allow the core solvent to diffuse readily through the shell liquid. The ability to control the formation of ribbons versus core/shell fibers through the design of the relative solidification times of the component fluids has significance beyond the current technology. By avoiding the use of specially designed needles or closely-spaced spinnerets, the potential for scale up and production of electrospun core/shell fibers in large quantities is greatly enhanced. This enabling technology opens up new opportunities for core/shell fibers in fields as diverse as tissue engineering and drug delivery, biosensors and environmental monitoring, catalysis and reaction engineering, and energy storage.

Acknowledgments

This research was funded by Novartis-MIT Center for Continuous Manufacturing.

References

Donahue, D.J., Bartell, F.E., 1985. The boundary tension at water-organic liquid interface. J. Phys. Chem. 56, 480-484.

Forward, K.M., Rutledge, G.C., 2012. Free surface electrospinning from a wire electrode. Chem. Eng. J. 183, 492-503.

Fredenslund, A. 1979. Vapor-liquid equilibria using UNIFAC: A group contribution method, Elsevier Scientific Pub. Co, New York, 1979.

Fridrikh, S.V., Yu, J.H., Brenner, M.P., Rutledge, G.C., 2003. Controlling the fiber diameter during electrospinning. Phys. Rev. Lett. 90, 144502.

Geller, A.S., Lee, S.H., Leal, L.G., 1986. The creeping motion of a spherical particle normal to a deformable interface. J. Fluid Mech. 169, 27-69.

Jirsak, O., Sysel, P., Sanetrnik, F., Hruza, J., Chaloupek, J., 2010. Polyamic acid nanofibers produced by needleless electrospinning. J. Nanomaterials 2010 ID842831.

Kase, S., Matsuo, T., 1965. Studies on melt spinning I. Fundamental equations on the dynamics of melt spinning. J. Poly. Sci. 3, 2541- 2254 (1965).

Koombhongse, S., Liu, W., Reneker, D.H., 2001. Flat polymer ribbons and other shapes by electrospinning. J. Polymer Sci. B 39, 2598-2606.

Kostakova, E., Meszaros, I., Gregr, J., 2009. Composite nanofibers produced by modified needleless electrospinning. Mater. Lett. 63, 2419-2422.

Li, D., Xia, Y.N., 2004. Direct fabrication of composite and ceramic hollow nanofibers by electrospinning. Nano Lett. 4, 933-938.

Liu; Y., He, J-.H., 2007. Bubble elecrtospinning for mass production of nanofibers. Int. J. Nonlinear Sci. Num. Simulation 8, 393-396.

Longson, T. J., Bhowmick R., Gu, C., Cruden, B. A., 2001. Core-shell interactions in coaxial electrospinning and impact on electrospun multiwall carbon nanotube core, poly(methyl methacrylate) shell fiber. J Phys. Chem. C 115, 12742-12750.

McCann, J.T., Li, D., Xia Y., 2005. Electrospinning of nanofibers with core-sheath, hollow, or porous structure. J. Mater. Chem. 15, 735-738.

Miloh, T., Spivak, B., Yarin, A.L., 2009. Needleless electrospinning: electrically driven instability from the free surface of a spherical liquid layer. J. Appl. Phys. 106, 114910-114910-8.

Moghe, A.K., Gupta, B.S., 2008. Co-axial electrospinning for nanofiber structures: Preparation and applications. Poly. Rev. 48, 353-377.

National Institute of Health, 2012. http://rsb.info.nih.gov/ij/.

Niu, H., Lin, T., Xang, X., 2009. Needleless electrospinning: A comparison of cylinder and disk nozzles. J. Appl. Poly. Sci. 114, 3524-3530.

Niu, H., Lin, T. Fiber generator in needleless electrospinning. J. Nanomaterials 2012, 725950.

Pai, C.-L., Boyce, M.C., Rutledge, G.C., 2009. Morphology of porous and wrinkled fibers of polystyrene electrospun from dimethylformamide. Marcomolecules 42, 2102-2114.

Pan, C., Ouyang, G., Lin, J., Rai, T., Zhen, X., Lu, G., Huang, Z., 2004. Excess Molar Volumes and Surface Tensions of 1,2,4-Trimethylbenzene and 1,3,5-Trimethylbenzene with 1-Butanol, 2-Methyl-1-propanol, 2-Butanol, and 2-Methyl-2-propanol at 298.15 K, J. Chem. Eng. Data 49, 1744-1747.

Quéré, D., 1999. Fluid coating on a fiber. Ann. Rev. Fluid Mech. 31, 347-384.

Rutledge, C. G., Fridrikh, S.V., 2007. Formation of fibers by electrospinning. Adv. Drug Deliv. Rev. 59, 1384-1391.

Saville, D. A., 1997. Electrohydrodynamic: The Taylor-Melcher Leaky Dielectric Model Ann. Rev. Fluid Mech. 29, 27-64.

Skrzecz, A., Shaw, D., Maczynski, A., 1999. IUPAC- NIST solubility data series 69. Ternary alcohol-hydrocarbon-water systems. J. Phys. Chem. Ref. Data, 28, 983-1090.

Sun, Z.C., Zussman, E., Yarin, A.L., Wendroff, J.H., Greiner, A., 2003. Compound core-shell polymer nanofibers by co-electrospinning. Adv Mater 15, 1929–193

Theron, S.A., Zussman, E., Yarin, A.L., 2004. Experimental investigation of the governing parameters in the electrospinning of polymer solutions. Polymers 45, 2017-2030.

Theron, S.A., Yarin, A.L., Zussman, E., Kroll, E., 2005. Multiple jets in electrospinning: Experiment and modeling. Polymer 46, 2889-2899.

Wang, L., Pai, C.-L., Boyce, M.C., Rutledge G.C., 2009. Wrinkled surface topographies of electrospun polymer fibers. Appl. Phys. Lett. 94, 151916-151916-3.

Varabhas, J.S., Tripatanasuwan, S., Chase, G.G., Reneker D.H., 2009. Electrospun jets launched from polymeric bubbles. J. Engin. Fibers Fabrics 4, 46-50.

Yan, X., Freyman, T., Pham. Q., Marini, J., Mulligan, R., Sharma, U., Brenner, M.P., Rutledge, G.C., 2012. High-throughput needleless electrospinning of core-sheath fibers, Fiber Society 2012 Annual Meeting, Boston, MA USA, November 7-9th 2012.

Yarin, A.L., Koombhoungse, S., Reneker, D.H., 2001.Bending instability in electrospinning of nanofibers. J. Appl. Phys. 89, 3018 – 3026.

Yarin, A.L. Zussman, E., 2004. Upward needleless electrospinning of multiple nanofibers. Polymers 45, 2977-2980.

Yarin, A.L., 2011. Coaxial electrospinning and emulsion electrospinning of core-shell fibers. Poly. Adv. Technol. 22, 310-317.

Yu, J.H., Fridrikh, S.V., Rutledge, G.C., 2004. Production of submicrometer diameter fibers by two-fluid electrospinning. Adv. Mater. 16, 1562.

Appendices

A. Properties of solutions examined in this work

Table A.1 Properties of the top (shell) solution.

PS molar mass, concentration, C_T	Solvent composition[a]	Density, ρ_T (g/mL)	Conductivity (μS/cm)	Zero shear rate viscosity (mPa s)	Surface tension[b] (mN/m)	Interfacial tension with water[c] (mN/m)
35kDa, 10wt%	0:100	0.89	<0.01	3.0	28.1	39.5
	10:90	0.88	<0.01	3.0	27.8	14.6
	20:80	0.88	<0.01	3.0	27.4	12.3
	35:65	0.87	<0.01	2.8	26.6	8.5
35kDa, 20wt%	0:100	0.92	<0.01	11	28.1	39.5
	10:90	0.91	<0.01	11	27.8	14.6
	20:80	0.91	<0.01	11	27.4	12.3
	35:65	0.90	<0.01	10	26.6	8.5
35kDa, 30wt%	0:100	0.93	<0.01	44	28.1	39.5
	10:90	0.92	<0.01	44	27.8	14.6
	20:80	0.92	<0.01	43	27.4	12.3
	35:65	0.92	<0.01	42	26.6	8.5
35kDa, 35wt%	35:65	0.95	<0.01	100	26.6	8.5
35kDa, 40wt%	35:65	0.97	<0.01	190	26.6	8.5

[a] weight of n-butanol and mesitylene in the solvent.

[b] Pan et al., 2004

[c] Donahue and Bartell, 1952

Table A.2: Properties of the bottom (core) solution

Solute, molar mass, Concentration, C_B	Solvent	Density, ρ_B (g/mL)	Conductivity (μS/cm)	Viscosity @ 200 s^{-1} (mPa s)
PEG, 35kDa, 8.25wt% PEO, 300kDa, 3.75wt%	Water	1.04	76.7	330
PVP, 360kDa, 15wt%	Water	1.04	6.8	550
PVP, 1.3MDa, 8wt%	Water	1.02	7.3	90

B. Mass Transport Model

The model consists of a the circular cross-section of a cylindrical element composed of two liquids arranged in a coaxial configuration such that there is an inner (core) liquid and an outer (shell) liquid, as shown in Figure B.1. The model is axially symmetric, with concentration gradients only in the radial direction. Convection and thinning of the cylindrical element due to elongation are neglected in this model. Each liquid is composed of a nonvolatile solute and one or more volatile solvents with known initial concentrations. Also specified is the initial jet radius ratio $\varepsilon_{j0} = R_I/R_O$ where R_I is the initial radius at the interface between the core and shell components, and R_O is the initial radius of the outermost surface of the cylindrical assembly. The jet radius ratio is set initially to correspond to a chosen value of bottom fluid fraction in the jet, v_B; R_O = 1 micron was chosen to accord approximately with the terminal jet radius (Fridrikh et

al., 2003). All solvents diffuse to the outermost surface of the cylindrical assembly, where they are removed by evaporation. As evaporation takes place, the respective volumes of the core and shell liquids (and hence also the diameters of the core and shell) decrease until solidification occurs. Solidification is defined as that point where either phase reaches a total solvent concentration less than 10 vol%. The purpose of the model is to determine the solidification times of the core and shell phases, denoted t_c and t_s, respectively. When $t_c > t_s$ the shell phase solidifies first, producing ribbons or collapsed fibers. When $t_s > t_c$ the core phase solidifies first, producing the desired solid core/shell fibers.

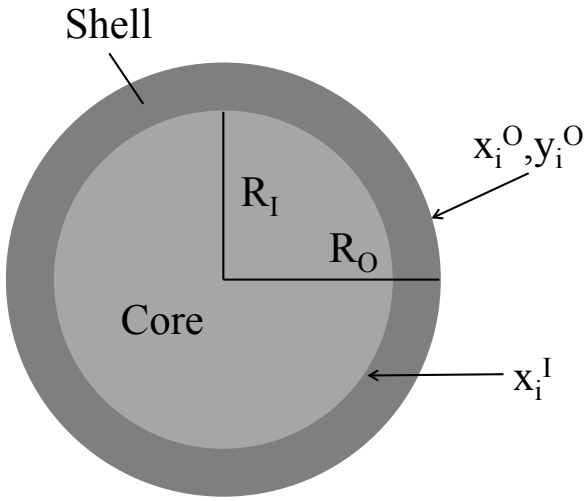

Figure B.1. Schematic of the proposal model

The diffusive mass flux J_i^D of solvent *i* through the outer fluid is described by Fick's first law:

$$J_i^D = D_i A_m \frac{\left(x_i^I - x_i^O\right)}{R_O - R_I} \qquad \text{Eq. (B.1)}$$

where D_i is the diffusivity, A_m is the logarithmic mean area, x_i^I is the concentration at the interface between the core and shell phases, and x_i^O is the concentration at the outermost surface of the shell phase. The diffusivities of water in n-butanol (0.93×10^{-5} cm^2/s) and in mesitylene (0.723×10^{-5} cm^2/s) are relatively similar; thus the diffusivity of water through the outer phase was assumed to be 1×10^{-5} cm^2/s regardless of composition; the effect of the polymer concentration on diffusivities was also assumed to be negligible. The concentration of core solvent on the shell side of the liquid-liquid interface was determined using solubility data obtained from the literature.

The solvent concentrations in the vapor phase at the outermost surface of the jet are functions of the evaporation rate of the solvents at the outer surface. The evaporative flux J_i^E for solvent *i* was determined by the mass transfer equation:

$$J_i^E = h_i \rho A\left(y_i^O - y_i^\infty\right) \qquad \text{Eq (B.2)}$$

where h_i, ρ, A, y_i^O, and y_i^∞ are, respectively, the mass transfer coefficient, density of the vapor phase (assuming an ideal gas), area of the outer surface, mole fraction in the vapor phase at the

outer surface and mole fraction in the vapor phase at a distance far away from the surface. For the case where the ambient air flow is parallel to the jet axis, the Sherwood number is estimated by the following correlation (Yarin et al., 2001):

$$Sh = \frac{2R_O h_i}{D_i} = 0.495\,\mathrm{Re}^{1/3}\,Sc^{1/2} \quad . \qquad \text{Eq. (B.3)}$$

Here, Re (= $2\rho u R_O/\eta$) is the Reynolds number and Sc (= $\eta/\rho^l D_i$) is the Schmidt number. u, and η are the velocity of the ambient air relative to the jet (assumed to 1 m/s) and the viscosity of air, respectively. This correlation has been shown to be valid in air for Reynolds numbers from 0.5 to 50 (Kase and Matsuo, 1965). Here, we have assumed that this correlation can be extended to Reynolds numbers between 0.1 and 0.5.

Liquid-vapor equilibrium was assumed to exist for solvent i at the outer surface of the jet. A modified Raoult's equation was used to calculate the equilibrium concentrations, according to Eq. (B.4):

$$y_i^O P = \gamma_i x_i^O P_i^{sat} \qquad \text{Eq (B.4)}$$

where P, γ_i, and P_i^{sat} are the pressure, activity coefficient, and saturation vapor pressure, respectively. There are several methods to determine the activity coefficient of solvents systems; here we chose the Universal Functional Activity Coefficient (UNIFAC) model (Fredenslund, 1979) to calculate the activity coefficient of each solvent. The activity coefficient of each solvent is dependent on the concentration of the all the solvents in both liquid and vapor phases.

Given Eqs. (B.1) – (B.4), the computational algorithm shown in Fig. B.2 was used to calculate the times for solidification of the core and shell. Initially, the "set" variables are programmed into the routine; these include temperature, pressure, solubility data, saturated vapor pressure, etc. which are dependent on the solvent system used in the model. These "set" variables were the same for all cases considered in this work, since the same solvent system (n-butanol, mesitylene and water) were used in all of the experiments. The "input" variables are the initial concentrations of the solvents and non-volatile (polymer solute) components in each fluid, fluid densities and initial radius ratio. Based on the "set" and "input" variables, the volume and number of moles of each species were determined for each liquid phase. In addition, the equilibrium concentration at the interface of the two fluids was calculated from the solubility data. After the mass transfer coefficient was determined, an initial guess was made for the concentration of each solvent at the outer surface, and the diffusive and evaporative fluxes were calculated. The surface concentrations were then refined iteratively until the diffusive and evaporative fluxes were equal for all volatile components (solvents). Once the fluxes were determined, a small step forward in time was taken, and the radii of the interface and outermost surface were updated to account for the change in volume due to diffusion and evaporation. This constitutes one pass through the calculation. The fluxes where then recalculated, and the program iterated forward in time until the solvent volume of either fluid was less than 10% of the initial solvent volume.

The ambient environment was assumed to be at a temperature of 25 C, a pressure of 1 atm and a relative humidity of 0%. The time step was 0.01 ms.

An example calculation is provided below for the case where the top liquid is 20w% PS in a mixed solvent of 20:80wt% of n-butanol:mesitylene and the bottom liquid is 12wt% PEG+PEO (73:27wt% mixture) in DI water. Table B.1 shows the input variables for the model, which depend on the initial jet radius ratio and solution properties. These variables were varied for the different systems examined in this study. Table B.2 displays the set variables, which were not changed throughout this study. In addition, the ternary phase equilibrium data for water, n-butanol and mesitylene from Skrzecz *et al.* (Skrzecz et al., 1999) was used to determine the equilibrium composition of the organic and aqueous phases. If different solvents had been examined, the diffusivity, saturated vapor pressure and density of the solvents would have become input variables.

Table B.1. The input variables for a system in which the top liquid is 20w% PS in a mixed solvent of 20:80wt% of n-butanol:mesitylene and the bottom liquid is 12wt% PEG+PEO (73:27wt% mixture) in DI water.

Input Variable	Value
Initial jet radius ratio, ε_{j0}	0.85
Initial composition of organic solvent (n-butanol:mesitylene)	20:80wt%
Solute concentration in	
top fluid (polystyrene, 35kDa)	20 wt%
bottom fluid (polyethylene glycol, 35kDa and polyethylene oxide, 300kDa, 73:27wt% mixture)	12 wt%
Density of solution	
top fluid	910 kg/m^3
bottom fluid	1040 kg/m^3
Density of solidified polymer	
top solute (polystyrene)	1050 kg/m^3
bottom solute ((polyethylene glycol, 35kDa and polyethylene oxide, 300kDa, 73:27wt% mixture)	1150 kg/m^3

Table B.2. The set variables for the mass transfer model.

Set Variable	Value
Temperature	25 °C
Pressure	101 kPa
Kinematic viscosity of air	0.15×10^{-6} m^2/s
Relative humidity	0 %
Initial outer jet diameter	1 μm
Jet velocity	1 m/s
Diffusion coefficient	
n-butanol in air	0.80×10^{-5} m^2/s
mesitylene in air	0.62×10^{-5} m^2/s
water in air	2.82 x 10-5 m2/s
water in organic shell	1.0×10^{-9} m^2/s
Density of solvent	
n-butanol	810 kg/m^3
mesitylene	864 kg/m^3
Water	1000 kg/m^3
Saturated Vapor Pressure at 25C	
n-butanol	820 Pa
mesitylene	320 Pa
Water	3100 Pa

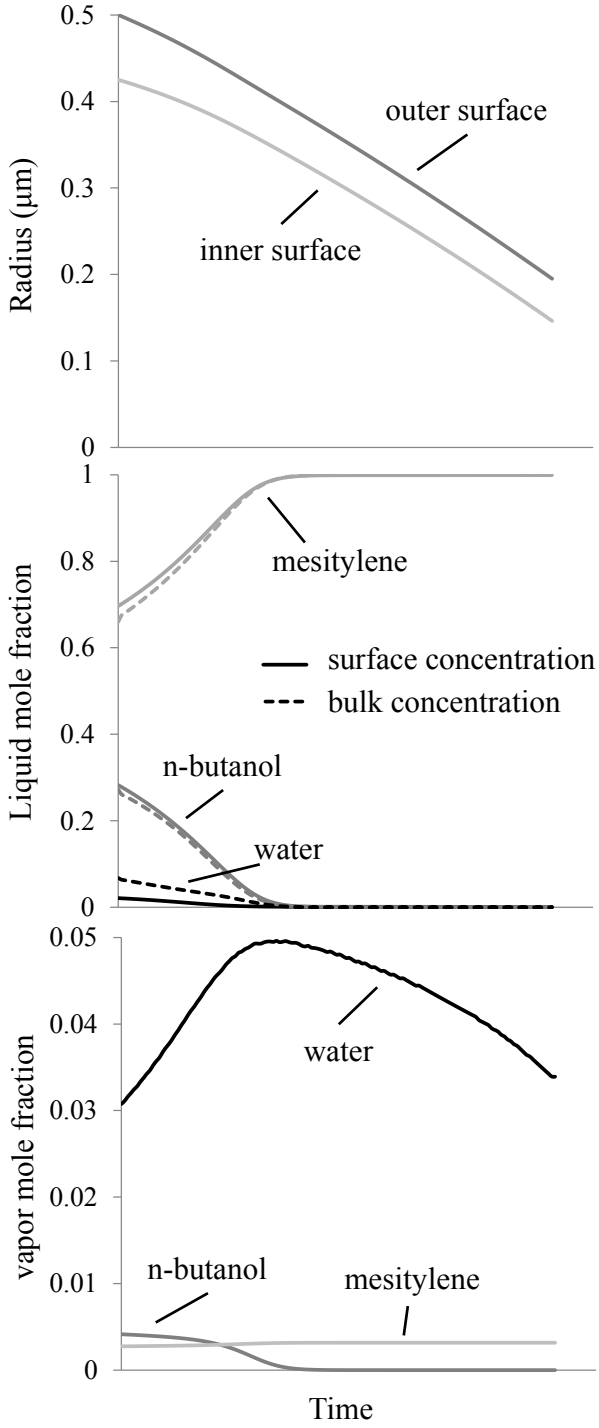

Figure B.2. Model results for the system where the top liquid was 20w% PS in a solvents of 20:80wt% of n-butanol:mesitylene and bottom liquid was 12wt% PEG+PEO (73:27wt% mixture) in DI water. (a) Variation in core and shell radii, R_I and R_O, respectively, with time as solvents evaporate from the jet. (b) Mole fractions of solvents in the shell phase as function of time. "surface" refers to the concentration at R_O, where evaporation occurs and "bulk" refers to average mole fraction of solvent in the shell phase. (c) Mole fractions of solvent in the vapor

immediately in contact with the jet. This vapor is assumed to be in equilibrium with the liquid at the jet surface.

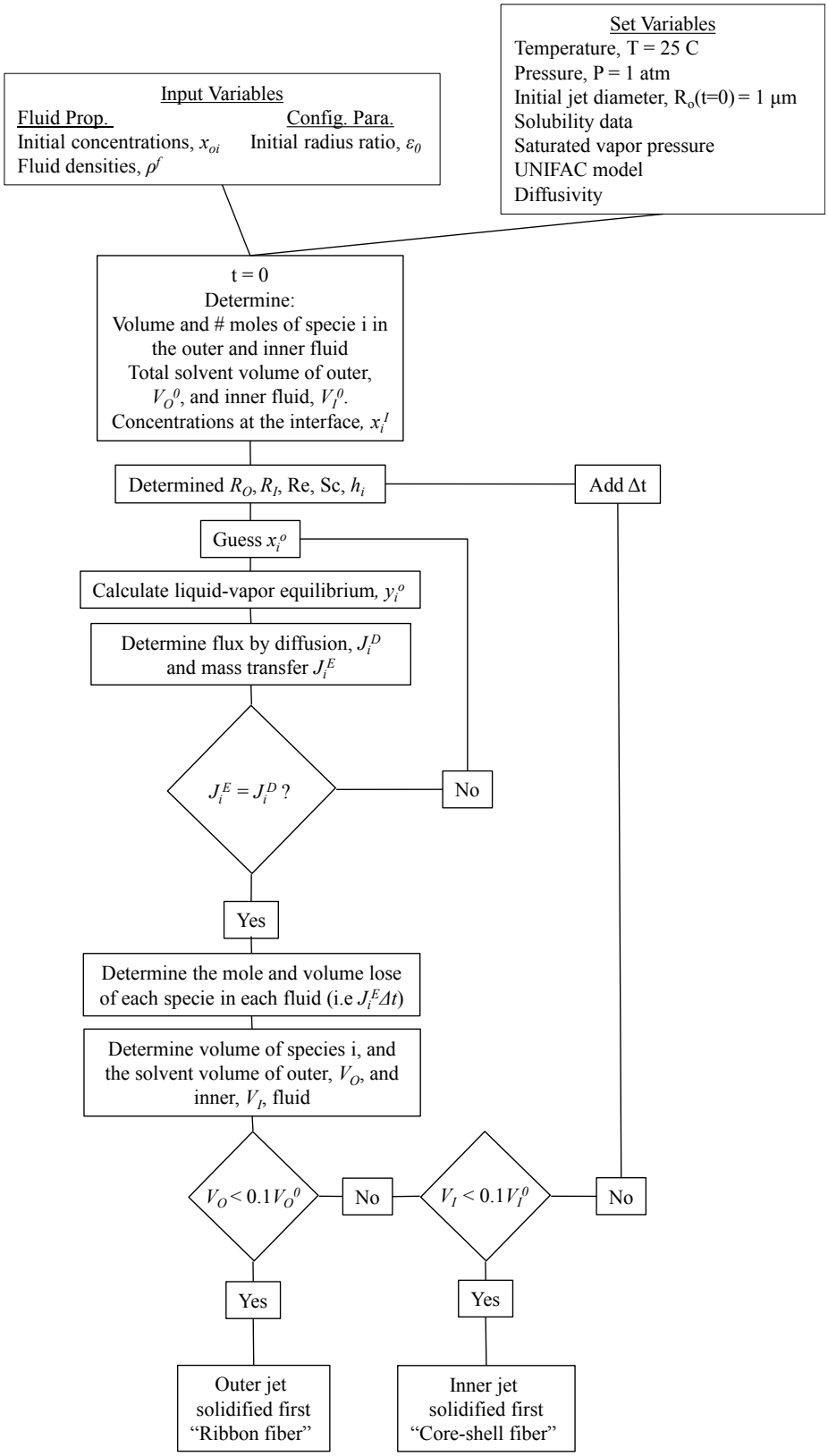

Figure B.3. Flow diagram of the computation routine.